



## Short communication

## Manganese dioxide nanorod arrays on carbon fabric for flexible solid-state supercapacitors



Minghao Yu<sup>a</sup>, Teng Zhai<sup>a</sup>, Xihong Lu<sup>a,\*\*</sup>, Xiaojun Chen<sup>a,b</sup>, Shilei Xie<sup>a</sup>, Wei Li<sup>a</sup>,  
Chaolun Liang<sup>a,c</sup>, Wenxia Zhao<sup>c</sup>, Liping Zhang<sup>b</sup>, Yexiang Tong<sup>a,\*</sup>

<sup>a</sup> KLGHEI of Environment and Energy Chemistry, MOE of the Key Laboratory of Bioinorganic and Synthetic Chemistry, School of Chemistry and Chemical Engineering, Sun Yat-Sen University, Guangzhou 510275, People's Republic of China

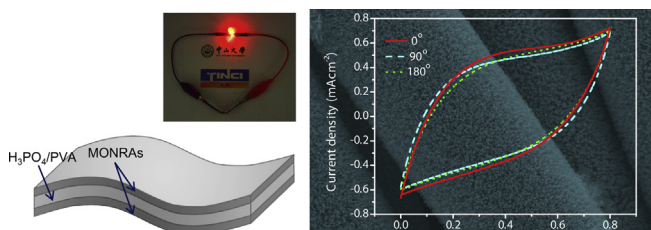
<sup>b</sup> Battery Material Business Division, Guangzhou Tinci Materials Technology Co., Ltd., Guangzhou 510760, People's Republic of China

<sup>c</sup> Instrumental Analysis and Research Centre, Sun Yat-Sen University, Guangzhou 510275, People's Republic of China

## HIGHLIGHTS

- Controllable growth of MnO<sub>2</sub> nanorods on 3D conductive carbon cloth.
- The MnO<sub>2</sub> nanorods achieved a high specific capacitance of 678 F g<sup>-1</sup> at 0.3 A g<sup>-1</sup>.
- A flexible and solid-state supercapacitor based on MnO<sub>2</sub> has been demonstrated.
- The fabricated device exhibited good electrochemical performance.

## GRAPHICAL ABSTRACT



## ARTICLE INFO

## Article history:

Received 15 October 2012

Received in revised form

7 March 2013

Accepted 11 March 2013

Available online 29 March 2013

## Keywords:

Flexible  
Manganese dioxide  
Nanorods  
Supercapacitors

## ABSTRACT

We reported the synthesis of large-area manganese oxide nanorods (MONRAs) on carbon fabric and their implementation as flexible supercapacitors. Electrochemical measurements demonstrated that MONRAs exhibited a high capacitance (678 F g<sup>-1</sup> at a current density of 0.3 A g<sup>-1</sup>) with high flexibility and excellent cycle performance (less than 3% capacitance loss after 10,000 cycles). Furthermore, the fabricated solid-state devices based on these MONRAs electrodes exhibited good electrochemical performance and could power a red LED well for about 5 min after charging at 0.5 mA cm<sup>-2</sup> for 30 s, with an energy utilization efficiency of about 80%. These findings show that MONRAs are a kind of very promising electrode material for flexible supercapacitors.

Crown Copyright © 2013 Published by Elsevier B.V. All rights reserved.

## 1. Introduction

Increasing power and energy demands for next-generation portable and flexible electronics such as roll-up displays, photovoltaic cells, and wearable devices have inspired intensive efforts to

explore flexible, lightweight and environmentally friendly energy storage devices [1–4]. Supercapacitors, also known as electrochemical capacitors, have received considerable attention as novel flexible energy storage devices, due to their unique power and energy densities [5–9]. On the basis of the different charge storage mechanisms, supercapacitors are classified into electrical double-layer capacitors (EDLCs) [10–12] and pseudocapacitors [13–17]. Compared to EDLCs, pseudocapacitors based on metal oxides or conducting polymers are more attractive because they can provide much higher capacitance and energy density through Faradic reaction [13–17]. Among various pseudocapacitive

\* Corresponding author. Tel.: +86 20 84110071; fax: +86 20 84112245.

\*\* Corresponding author.

E-mail addresses: [ce04lxh@mail2.sysu.edu.cn](mailto:ce04lxh@mail2.sysu.edu.cn) (X. Lu), [chedhx@mail.sysu.edu.cn](mailto:chedhx@mail.sysu.edu.cn) (Y. Tong).

materials, manganese dioxide ( $\text{MnO}_2$ ) has been considered to be the most attractive candidate in terms of its superior capacitor performance, low cost, environmentally friendly nature, and natural abundance. However, due to its poor electric conductivity ( $10^{-5}$ – $10^{-6} \text{ S cm}^{-1}$ ), the theoretical capacitance ( $1370 \text{ F g}^{-1}$ ) has not been achieved [18–23]. One dimensional (1D) nanoarrays hold great attention as electrode materials because they can provide high interfacial area, short ion diffusion path and fast electrical pathways. The direct growth of nanoarrays on conductive substrates can facilitate the diffusion of active species and transport of electrons, and hence may further broaden their applications in energy storage device [24–26]. In this regard, considerable efforts have been paid to the preparation of 1D  $\text{MnO}_2$  nanoarrays, and significant advance has been achieved [18,20,21,27,28]. However, facile synthesis of large-area 1D  $\text{MnO}_2$  on conductive substrates is still a challenge. On the other hand, the investigation of flexible integrated supercapacitors based on pristine  $\text{MnO}_2$  is very limited.

We have recently demonstrated that the synthesis of large-area manganese oxide nanorod arrays on F-doped  $\text{SnO}_2$  coated glass (FTO) and Ti substrates through a simple electrodeposition method [18]. In this paper, we reported the growth of large-area manganese oxide nanorods (MONRAs) and nanowires (MONWs) on carbon fabric by expanding this method and their implementation as flexible supercapacitors. Carbon fabric was here chosen as the substrate mainly due to its cost-effectiveness, high conductivity, and excellent chemical stability. On the other hand, the flexible nature of carbon fabric is also preferable for designing a flexible device. Electrochemical measurements showed that MONRAs electrode exhibits an excellent specific capacitance as high as  $678 \text{ F g}^{-1}$  at a current density of  $0.3 \text{ A g}^{-1}$ . In addition, MONRAs electrode showed excellent long-term cycle stability. Furthermore, a demo of solid-state supercapacitor with high flexibility and good electrochemical capacitor performance was assembled. The tandem devices could power a red LED well for about 5 min after charging at  $0.5 \text{ mA cm}^{-2}$  for 30 s, with an energy utilization efficiency of about 80%.

## 2. Experimental

### 2.1. Synthesis of MONRAs and MONWs

All reagents used were of analytical grade and were used directly without any purification. Standard  $\text{MnO}_2$  and  $\text{Mn}_3\text{O}_4$  were purchased from Alfa Aesar. Both MONRAs and MONWs were fabricated by a template-free electrodeposition method in a simple three-electrode glass cell. Carbon fabric was used as working electrode. A Pt wire and a saturated calomel electrode (SCE) that connected to the cell with a double salt bridge were used as counter electrode and reference electrode, respectively. Anodic electrodeposition of MONRAs was performed at a constant current of  $0.4 \text{ mA cm}^{-2}$  in a solution containing 0.01 M manganese acetate ( $\text{MnAc}_2$ ) and 0.02 M ammonium acetate ( $\text{NH}_4\text{Ac}$ ). Anodic electrodeposition of MONWs was carried out at a constant current of  $0.4 \text{ mA cm}^{-2}$  in a solution containing 0.05 M  $\text{MnAc}_2$  and 0.02 M  $\text{NH}_4\text{Ac}$ . The temperature of both reactions was kept at  $70^\circ\text{C}$ .

### 2.2. Fabrication of solid-state device

The solid-state device was fabricated with two pieces of MONRA electrodes. A separator (NKK TF45,  $40 \mu\text{m}$ ) was placed between the two electrodes, and polyvinyl alcohol (PVA)– $\text{H}_3\text{PO}_4$  gel was used as a solid electrolyte. PVA– $\text{H}_3\text{PO}_4$  electrolyte was simply made as follows: 2 g  $\text{H}_3\text{PO}_4$  was mixed with 20 mL deionized water and then 2 g PVA powder was added. The whole mixture was heated up steadily to  $85^\circ\text{C}$  under vigorously stirring until the solution became

clear. Then the solution was kept at  $85^\circ\text{C}$  without stirring. Two pieces of carbon fabric with MONRAs were immersed in PVA– $\text{H}_3\text{PO}_4$  gel for 3 min with the bare carbon fabric part above the gel. Then they were took out and assembled together with a separator (NKK TF45,  $40 \mu\text{m}$ ) placed between them, leaving aside the bare carbon fabric part as the electrode. After the PVA– $\text{H}_3\text{PO}_4$  gel was solidified at room temperature, the solid-state device was prepared.

### 2.3. Characterization

The morphology, microstructure, and compositions of the products were characterized by field-emission scanning electron microscopy (FE-SEM, JSM-6330F), X-ray diffractometry (XRD, D8 ADVANCE), transmission electron microscopy (TEM, JEM2010-HR), laser Micro-Raman Spectrometry (Renishaw inVia), photoelectron Spectroscopy (XPS, ESCALab250). Inductively coupled plasma atomic emission spectroscopy (ICP, SPECTRO) was used to analyze the loading of manganese oxide on carbon fabric. The mass loading of MONRAs and MONWs is about  $0.31 \text{ mg cm}^{-2}$  and  $0.42 \text{ mg cm}^{-2}$ . The electrochemical properties of the products were investigated with cyclic voltammetry (CV), charge–discharge measurements and electrochemical impedance spectroscopy by employing a CHI 660D electrochemical workstation (Chenhua, Shanghai).

## 3. Results and discussion

Fig. 1(a) shows the optical image of the samples prepared by electrodeposition. A uniform gray film was formed on the surface of carbon fabric when the electrodeposition was carried out with a current density of  $0.4 \text{ mA cm}^{-2}$  in a solution containing 0.05 M  $\text{MnAc}_2$  and 0.02 M  $\text{NH}_4\text{Ac}$  (rectangle in Fig. 1(a)). The structure of the as-prepared MONWs and MONRAs was characterized by the SEM technique, as shown in Fig. 1(b)–(f). Fig. 1(b) and (c) clearly demonstrates that the well-established structure of MONWs was grown on carbon fibers. These nanowires have a diameter of 60–90 nm and length of up to several micrometers. Additionally, these nanowires interlace together to form a three-dimensional network. By contrast, a dark film consisting of a large number of uniform nanorods was obtained when the concentration of  $\text{MnAc}_2$  decreased to 0.01 M (dot rectangle in Fig. 1(a) and (d)). From Fig. 1(e)–(f), we can see that free-standing and dense nanorods of 50–100 nm in diameter and  $2.5 \mu\text{m}$  in length were grown uniformly on each carbon fiber. The result above indicates that the morphology of product can be readily controlled by simply varying the concentration of  $\text{MnAc}_2$  in electrodeposition process.

X-ray diffraction (XRD) patterns were collected from the nanowires and nanorods to study the crystal structure (Fig. S1a). To avoid that the peaks would be covered by the strong peak of carbon fabric, the prepared product were peeled off from the carbon fabric before the test. Some peaks are observed for MONRAs and MONWs. The peaks located at  $18.1^\circ$ ,  $36.7^\circ$ ,  $37.5^\circ$  and  $60.3^\circ$  in MONRAs can be indexed to tetragonal  $\text{MnO}_2$  (JCPDS # 44-0141), while all the peaks in MONWs can be well assigned to the tetragonal  $\text{Mn}_3\text{O}_4$  (JCPDS # 24-0734). In order to further analyze the chemical compositions, Raman spectra of MONRAs and MONWs were conducted and the standard  $\text{MnO}_2$  and  $\text{Mn}_3\text{O}_4$  samples were also examined in the same conditions. From Fig. 2(a), only one sharp peak at  $644 \text{ cm}^{-1}$  is observed for MONRAs, which is attributed to (Mn–O) symmetric stretching vibrations of  $\text{MnO}_6$  octahedron in  $\text{MnO}_2$  compounds [29,30]. Besides one sharp peak at  $660 \text{ cm}^{-1}$ , there are still three weak peaks at 316, 375 and  $552 \text{ cm}^{-1}$  in MONWs. All these peaks are in consistent with the stretching vibrations of  $\text{Mn}_3\text{O}_4$  [29,30]. Thus, the Raman results indicate that  $\text{MnO}_2$  is dominant in MONRAs while  $\text{Mn}_3\text{O}_4$  is dominant in MONWs, which is in agreement

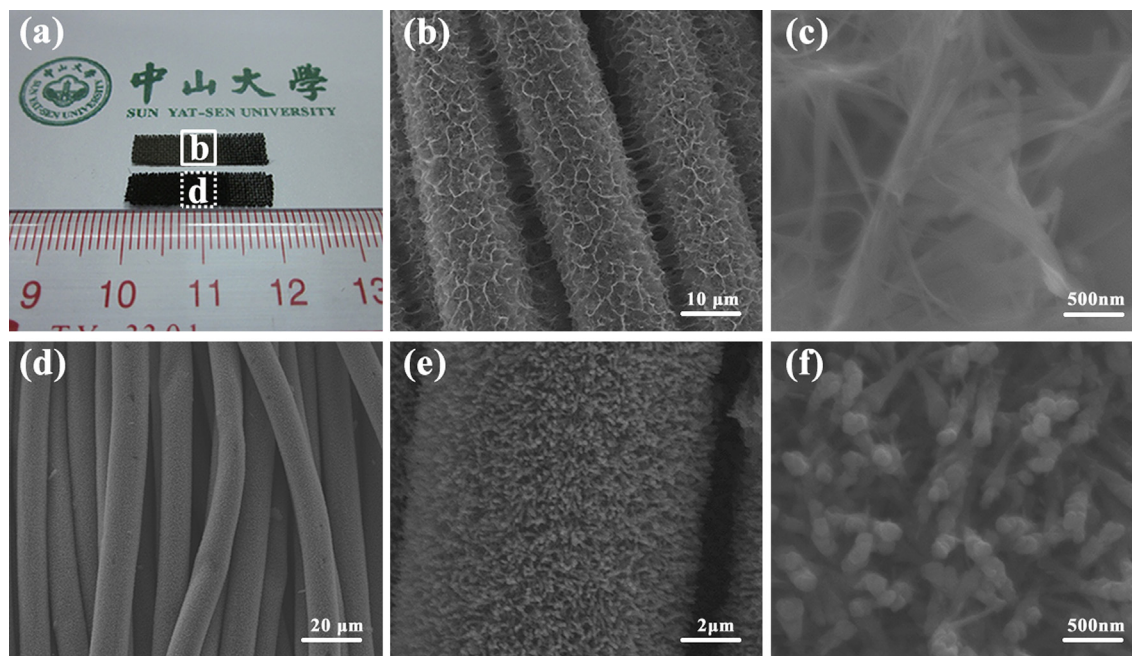


**Fig. 1.** (a) Optical image, (b, c) SEM images of MONWs grown on carbon fabric in a solution of 0.05 M  $\text{MnAc}_2 + 0.02$  M  $\text{NH}_4\text{Ac}$  with a current density of  $0.4 \text{ mA cm}^{-2}$  for 120 min at  $70^\circ\text{C}$ , (d, e, f) SEM images of MONRAs grown on carbon fabric in a solution of 0.01 M  $\text{MnAc}_2 + 0.02$  M  $\text{NH}_4\text{Ac}$  with a current density of  $0.4 \text{ mA cm}^{-2}$  for 120 min at  $70^\circ\text{C}$ .

with the XRD results and further confirmed by the XPS results. XPS survey spectra (Fig. S1b) demonstrate that Mn and O are present on the products and the C signal is attributed to adventitious carbon. Two peaks, corresponding to the Mn  $2p_{3/2}$  and Mn  $2p_{1/2}$  binding

energies, were observed in the Mn 2p spectra (Fig. 2(b)) [18,31]. The Mn  $2p_{3/2}$  peak at 641.9 eV for MONWs is attributed to the binding energy of  $\text{Mn}_3\text{O}_4$  and the peak at 642.3 eV for MONRAs is in accord with that of  $\text{MnO}_2$  [31]. Additionally, multiplet splitting Mn 3s peaks

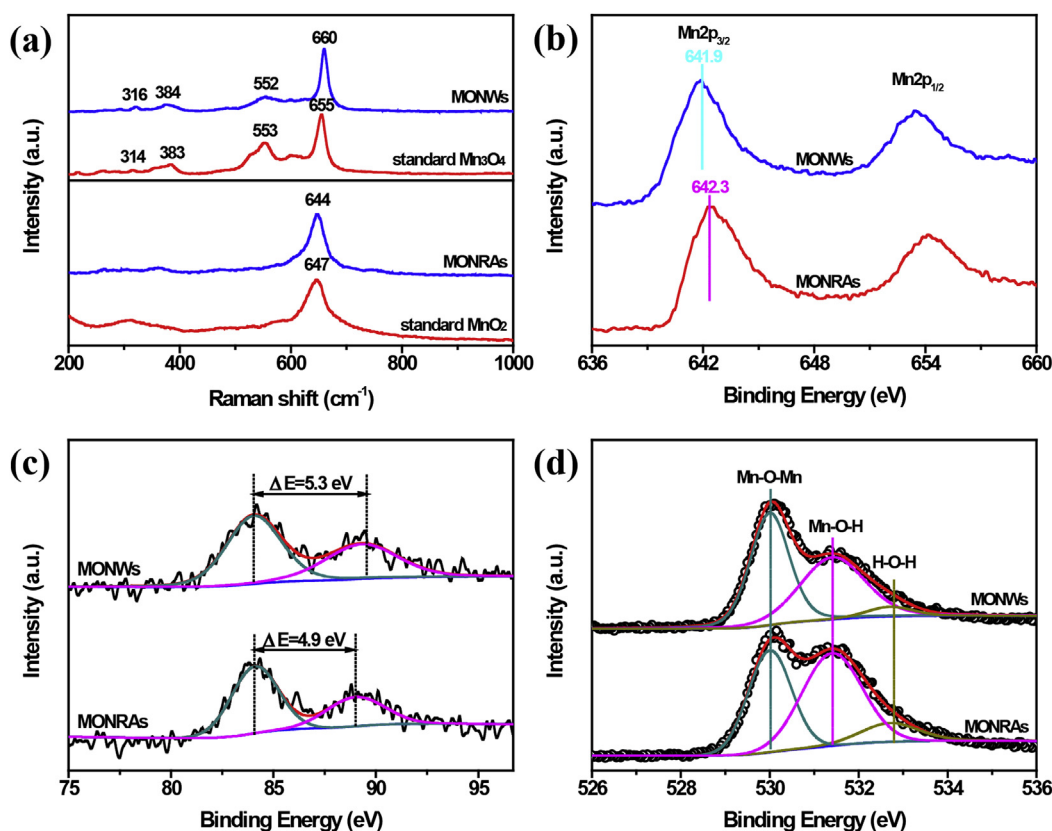


**Fig. 2.** (a) Raman spectra, (b) Mn 2p XPS spectra, (c) Mn 3s XPS spectra and (d) O 1s XPS spectra of MONRAs and MONWs.



are also useful for determining oxidation state of Mn, which are shown in Fig. 2(c). The peak separation of electrons in the core level with unpaired electrons in the valence band level is caused by the electron exchange interaction upon photoelectron ejection. Since a lower valence implies more electrons in the 3d orbital, more interaction can occur upon photoelectron ejection. Consequently, the energy separation ( $\Delta E$ ) between the two components of the Mn 3s multiplet will increase [31]. The obtained  $\Delta E$  for MONWs and MONRAs is 5.3 eV and 4.8 eV, which are respectively consistent with  $\text{Mn}_3\text{O}_4$  and  $\text{MnO}_2$  reported before [32,33]. Fig. 2(d) shows the O 1s spectra of MONRAs and MONWs. The spectra can be de-convoluted into three components corresponding to the Mn–O–Mn (530.0 eV) for oxide, Mn–O–H (531.4 eV) for hydroxide and H–O–H (532.7 eV) for residual water respectively [34,35].

The detailed microstructure of MONRAs and MONWs has been further analyzed by transmission electron microscopy (TEM). The low-magnification TEM image (shown in Fig. 3(a)) clearly demonstrates MONRAs with diameters of about 60 nm is rough and some nanorods with a diameter of  $\sim 5$  nm grow around the backbone. The selected-area electron diffraction (SAED) pattern (the inset in Fig. 3(a)) demonstrates the MONRAs have a good crystallinity. Fig. 3(b) and its inset show the HRTEM images of MONRAs. The lattice fringe spacing is measured to be 0.39 nm, which is consistent with the planes of tetragonal  $\text{MnO}_2$  (JCPDS # 44-0141). Fig. 3(c) is the typical TEM image of MONWs, showing MONWs have a

diameter of about 90 nm. The inset in Fig. 3(c) is the corresponding SAED pattern, indicating the high crystallinity of MONWs. The enlarged HRTEM image (inset in Fig. 3(d)) reveals two sets of lattice fringe with the spacings of 0.40 nm and 0.23 nm, corresponding to the planes of tetragonal  $\text{Mn}_3\text{O}_4$  (JCPDS # 24-0734). This confirms the composition of MONWs is  $\text{Mn}_3\text{O}_4$  again.

To investigate the electrochemical properties of MONRAs and MONWs, electrochemical measurements were conducted in a conventional electrochemical cell, with a Pt wire as counter electrode and a saturated calomel electrode (SCE) as reference electrode and 0.5 M  $\text{Na}_2\text{SO}_4$  aqueous solution as electrolyte. The correlation between the deposition time and specific capacitance for MONRAs was revealed as shown in Fig. S2. With the deposition time increasing, the deposition mass increased nearly proportionally, while the specific capacitance decreased accordingly. Fig. 4(a) compares the cyclic voltammogram (CV) curves of MONRAs electrode and MONWs electrode collected at a scan rate of  $100 \text{ mV s}^{-1}$ . In comparison with MONWs, MONRAs exhibit higher capacitive current density and a nearly rectangular CV shape, indicating the better electrochemical performance of MONRAs than MONWs. CV curves of MONRAs and MONWs at various scan rates with potential windows ranging from 0 to 0.8 V were also collected in Fig. S3. The quasi-rectangular and almost no significantly changed shapes of these curves as the scan rate increasing from 2 to  $200 \text{ mV s}^{-1}$  reveal the improved mass transportation and good rate capability of

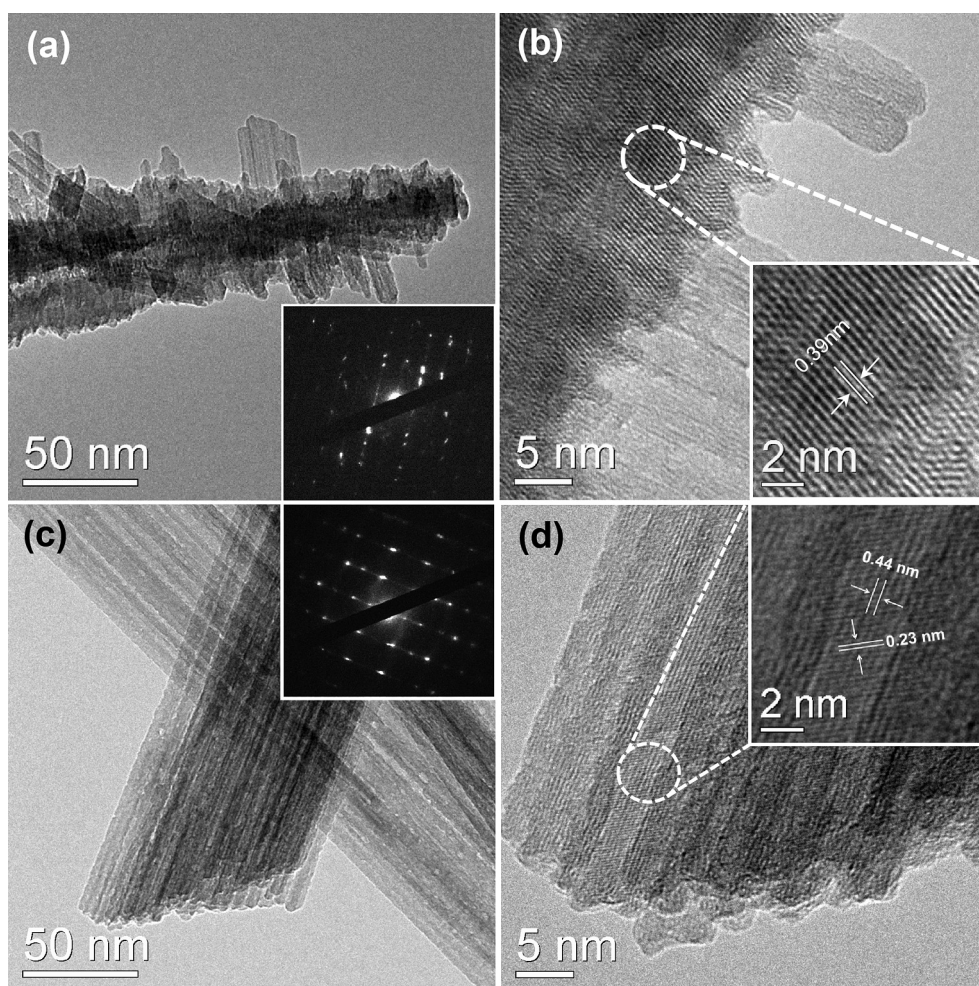


**Fig. 3.** (a) TEM image and (b) HRTEM image of MONRAs, (c) TEM image and (d) HRTEM image of MONWs. The insets in Fig. 3a and c are the corresponding SAED patterns of MONRAs and MONWs.

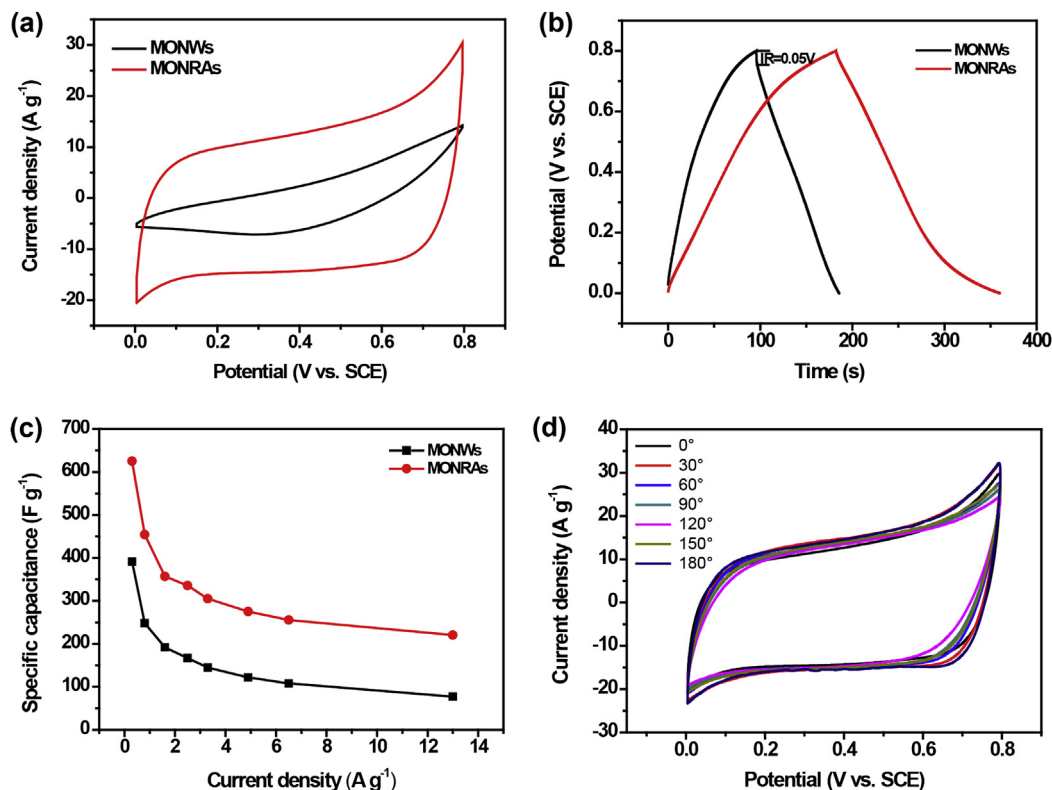


**Fig. 4.** (a) CV curves of MONRAs and MONWs obtained at a scan rate of 100 mV s<sup>-1</sup>. (b) Galvanostatic charge–discharge curves of MONRAs and MONWs collected at a current density of 1.6 A g<sup>-1</sup>. (c) Plotted curves of the variation in the specific capacitance for MONRAs and MONWs measured as a function of current density. (d) CV curves of MONRAs under different bending conditions.

MONRAs. The variation on the specific capacitance of MONRAs and MONWs as a function of the scan rate is also shown in Fig. S3c. The specific capacitance of MONRAs is substantially higher than MONWs at the same scan rate, again confirming the superior performance of MONRAs. For further evaluating the capacitive performance of MONRAs and MONWs, galvanostatic charge–discharge testing was carried out. Fig. 4(b) shows the charge–discharge curves of MONRAs and MONWs at a current density of 1.6 A g<sup>-1</sup>. Both their charge curves are relatively symmetric to their corresponding discharge curves, suggesting their good electrochemical behavior. The discharge curve of MONRAs is substantially prolonged over MONWs, again confirming the superior capacitive behavior of MONRAs. Moreover, the IR drop for MONRAs is negligible, which is much smaller than that of MONWs electrode (0.05 V), revealing the superior electrical conductivity of MONRAs. The specific capacitance for the electrodes can be obtained from charge–discharge data according to equation (1):

$$C = \frac{I\Delta t}{\Delta Vm} \quad (1)$$

where  $C$  (F g<sup>-1</sup>) is the specific capacitance,  $I$  (A) is the constant discharging current,  $\Delta t$  (s) is the discharging time,  $\Delta V$  (V) is the potential window, and  $m$  (g) is the mass loading of the active material in the working electrode (the mass loading for MONRAs and MONWs is about 0.31 mg cm<sup>-2</sup> and 0.42 mg cm<sup>-2</sup>). Fig. 4(c) summarized the specific capacitance of the two electrodes calculated from their discharge curves with different current densities. The specific capacitances for MONRAs are obviously higher than MONWs. The highest specific capacitance for MONRAs and MONWs achieved 625 F g<sup>-1</sup> and 386 F g<sup>-1</sup> at the current density of 0.3 A g<sup>-1</sup>, respectively. This value for MONRAs is comparable to

those recently reported for other nanostructured MnO<sub>2</sub> electrodes, such as MnO<sub>2</sub> nanowires (390 F g<sup>-1</sup> at 0.3 A g<sup>-1</sup>) [21], MnO<sub>2</sub> nanoflakes (328 F g<sup>-1</sup> at 0.5 A g<sup>-1</sup>) [36], hierarchical tubular MnO<sub>2</sub> structures (315 F g<sup>-1</sup> at 0.2 A g<sup>-1</sup>) [37], and MnO<sub>2</sub> nanotube arrays (349 F g<sup>-1</sup> at 1 A g<sup>-1</sup>) [38]. When the current density increases to 13 A g<sup>-1</sup>, the specific capacitance of MONRAs still remains about 35.2% (220 F g<sup>-1</sup>) comparable to that obtained at 0.3 A g<sup>-1</sup>, while only 20% (77 F g<sup>-1</sup>) for MONWs. Significantly, the rate capability of MONRAs electrode is substantially higher than that of MONWs electrode. The superior rate capability of MONRAs can be mainly due to their unique structure. The free-standing and ordered nanorods can not only provide a shorter electron transportation and ion diffusion pathway, but also facilitate the reaction of active species, and hence result in a good rate capability.

In order to examine the potential of our products for flexible energy storage, a MONRAs electrode was placed under constant mechanical stress and electrochemical measurements were performed in 0.5 M Na<sub>2</sub>SO<sub>4</sub> aqueous solution. The CV performance of this electrode under different bending conditions is shown in Fig. 4(d). The CV curves have no significant difference as the bending angle changed from 0 to 180°, indicating that there was almost no effect found on capacitive behavior and the electrode can be bent arbitrarily without capacitive loss. This remarkable performance can be attributed to the high mechanical flexibility of carbon fabric and the strong bonding between MONRAs and carbon fabric.

Beside high specific capacitance, good cycling performance is also one of the most important characteristics for high-performance supercapacitors. The long-term stability of the electrodes was examined by galvanostatic charge–discharge cycling at a current density of 6.5 A g<sup>-1</sup>. From Fig. 5(a), it is interesting to find that the specific capacitance for MONWs increases more than 60%

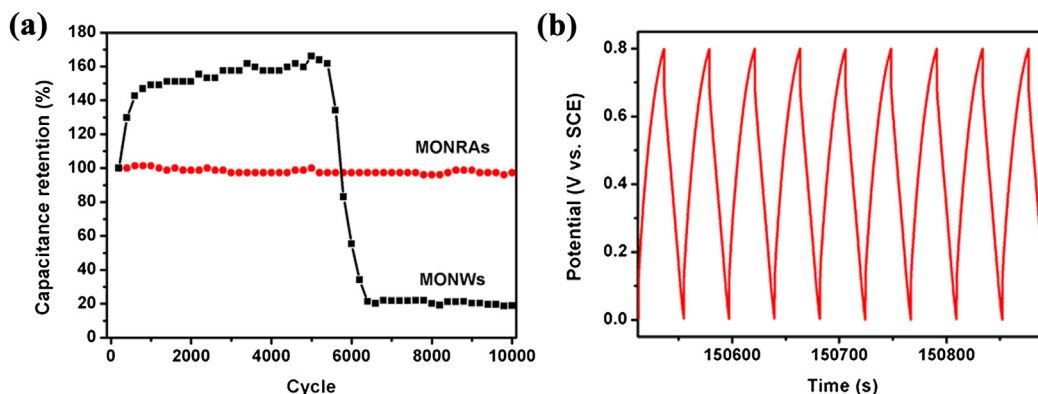


**Fig. 5.** (a) Capacitance retention of MONRAs and MONWs as a function of cycle number at a current density of  $6.5 \text{ A g}^{-1}$ . (b) Charge–discharge curves of MONRAs electrode in the potential range from 0 to 0.8 V at a current density of  $6.5 \text{ A g}^{-1}$ .

of the initial capacitance over the first 5000 cycles. The increasing of the specific capacitance may be due to the activation process of the electrode. After some circulations at the beginning, the intercalation and de-intercalation of the species will be more complete, leading to the increase of active points, hence enhances the specific capacitance. However, its capacitance dropped quickly at about 5500th cycle and only around 20% of the initial capacitance was retained after 10,000 cycles. This instability could be due to the structural modification of MONWs and bad contact between MONWs and carbon fibers (Fig. S4a). In contrary, MONRAs electrode exhibits an outstanding long-term stability, with less than 3% reduction of capacitance after 10,000 cycles. The cycling performance is higher than the results recently reported for  $\text{MnO}_2$  nanowires (12% decay after 3000 cycles) [21],  $\text{MnO}_2$  nanotube arrays (19% decay after 2000 cycles) [38], and Hierarchical tubular  $\text{MnO}_2$  structures (10% decay after 2000 cycles) [37]. From the SEM images (Fig. S4b), we could see that there is no obvious structural modification after 10,000 cycles. Thus, the excellent cycling performance for MONRAs is attributed to their good structural stability and contact between MONRAs and carbon fibers.

To better study these electrodes, electrochemical impedance spectroscopy (EIS) measurement was also conducted. Fig. 6 shows Nyquist plots recorded for MONRAs and MONWs, which were measured over a frequency range from 100 KHz to 0.1 Hz. A single semicircle in the high-frequency region and a sloping line in the low-frequency region could be observed clearly. The data can be nicely fit with the equivalent circuit as shown in the inset of Fig. 6. The  $R_e$  values for MONRAs ( $14.5 \Omega$ ) and MONWs ( $14.4 \Omega$ ) are almost the same, which means that the electrodes obtained by different

materials have the same combination resistance of electrolyte, intrinsic resistance of active materials, and contact resistance at the active material/current collector interface. The calculated  $R_{ct}$  values accounting for the charge-transfer resistance are in the order of MONRAs ( $4.4 \Omega$ ) < MONWs ( $11.5 \Omega$ ). That may be because the vertically aligned MONRAs provide much shorter paths for the transport of electron and the diffusion of species than the relatively disordered MONWs as indicated in Fig. 1(c) and (f). Additionally, Warburg resistance ( $Z_w$ ) corresponds to the frequency dependence of ion diffusion/transport in the electrolyte to the electrode surface. The higher  $Z_w$  value for MONRAs ( $0.035 \Omega$ ) than MONWs ( $0.005 \Omega$ ) means that the forming speed of the electric double-layer for MONRAs is faster. From the above analysis, it can be concluded that MONRAs have a superior capacitive behavior, which is in consistent with the electrochemical measurement conducted above.

To test their feasibility for flexible energy storage device application, a simple solid-state device based on MONRAs was also fabricated, and Fig. 7(a) shows the schematic illustration of the device. The as-fabricated device was lightweight and so highly flexible that it can be even twisted and folded without any detriment of the structural integrity. More importantly, the electrochemical performances of the device have no obvious change under various bending conditions (Fig. 7(b)). Fig. S5 displays the typical CV curves of this device. These CV curves showed a rectangular-like shape without obvious redox peaks and do not change significantly with the scan rate increasing, suggesting fast charge/discharge behavior of the device. Galvanostatic charge/discharge curves at various current densities were also recorded to further evaluate the performance of the device (Fig. 7(c)). Their charge curves are relatively symmetric to their corresponding discharge counterparts at the current densities from 0.1 to  $1 \text{ mA cm}^{-2}$ , further revealing the good capacitive behavior of the solid-state device. The long-term cycling stability of the device was tested through a cyclic charge/discharge process at a current density of  $1 \text{ mA cm}^{-2}$ . From Fig. 7(d), the device still retains about 76.5% of the initial capacitance after 5000 cycles. The decreased capacitance of the device might be due to the dissolution of  $\text{MnO}_2$  in  $\text{H}_3\text{PO}_4$ , and the stability may be improved by using the neutral solid-state electrolyte. Further work in improving its stability is in progress. Finally, we had connected two device units in series and found that the tandem devices could drive a red light-emitting diode (LED, 1.5 V) well for more than 5 min after charging at  $0.5 \text{ mA cm}^{-2}$  for 30 s (inset in Fig. 7(a)). According to this result, we also roughly calculated the energy storage efficiency of our devices. The theoretical storage energy of the tandem devices (two SCs) after charged at  $0.5 \text{ mA cm}^{-2}$  for 30 s is about  $3 \times 10^{-2} \text{ C}$  according to the equation:  $Q = It$ , where  $I$  is the charging current ( $I = 0.5 \text{ mA cm}^{-2} \times 2 \text{ cm}^2 = 1 \text{ mA}$ ),  $t$  is the

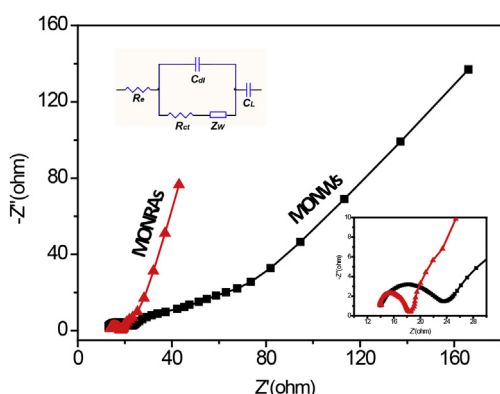


**Fig. 6.** Nyquist plots of MONRAs and MONWs. The inset is the equivalent circuit.



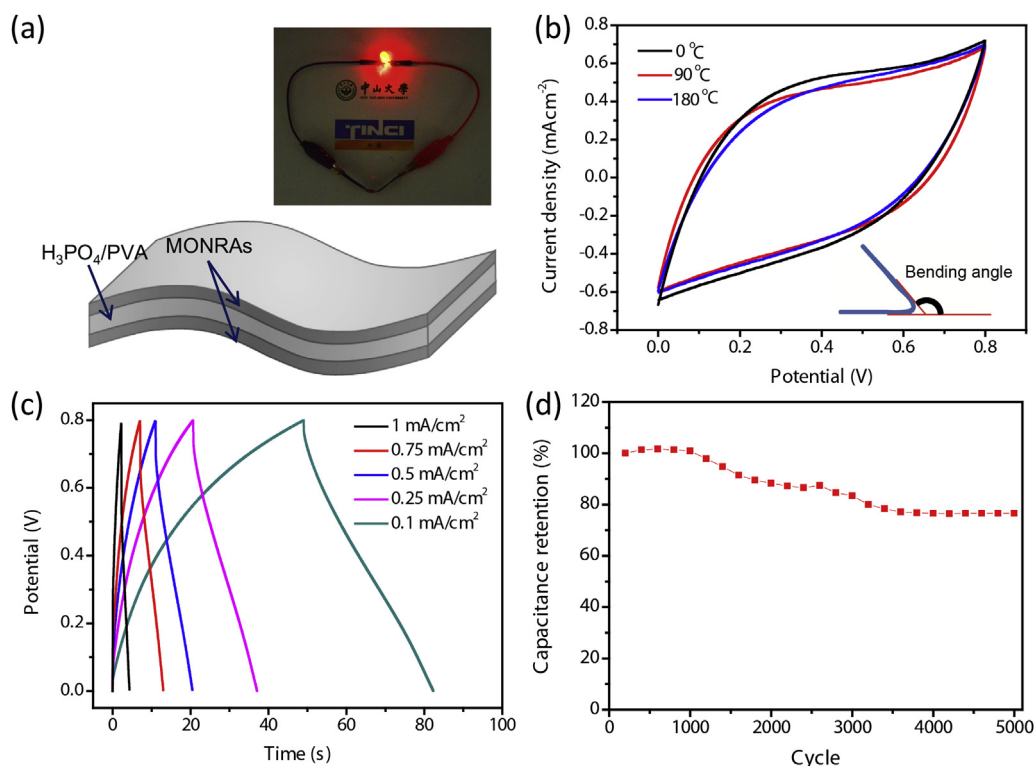


**Fig. 7.** (a) Schematic diagram of the solid-state symmetric device based on MONRAs electrodes with PVA/ $H_3PO_4$  polymer as electrolyte and separator. Inset: a digital photograph of light-emitting diode (LED) lighting demonstration, with the diode driven by two devices in series. (b) CV curves for a MONRAs supercapacitor at different curvatures of 0°, 90°, and 180°. (c) Galvanostatic charge–discharge curves for a MONRAs supercapacitor at different current density. (d) Cycling stability of a MONRAs supercapacitor over 5000 cycles at a current density of 0.5  $mAcm^{-2}$ .

charging time (30 s). The theoretical energy generated by lighting the LED is about  $2.4 \times 10^{-2}$  C based on the same equation ( $I = 8 \times 10^{-5}$  mA,  $t = 300$  s). Thus, about 80% of storage energy in the tandem devices could be utilized in powering the red LED.

#### 4. Conclusions

In summary, MONRAs and MONWs were successfully synthesized on flexible carbon fabric through a facile electrodeposition method. MONRAs show superior electrochemical performance to MONWs such as high specific capacitance and good cyclic stability. We also assembled a solid-state supercapacitor based on these MONRAs and found that the fabricated device could light a red LED well for more than 5 min after charging at 0.5  $mAcm^{-2}$  for 30 s, with an energy utilization efficiency of about 80%. These findings indicate that MONRAs electrode may have promising potential as the high-performance flexible supercapacitors.

#### Acknowledgments

Y. X. Tong acknowledges the financial support of this work by the Natural Science Foundations of China (90923008, 21273290 and J1103305), Strategic emerging industries in Guangdong Province (2011A010802004), the Integration of Production and Research Projects of the Ministry and Guangdong Province (2011B090400618), and the Research Fund for the Doctoral Program of Higher Education of China (No. 20120171110043). X. H. Lu thanks the Academic New Artist Ministry of Education Doctoral Post Graduate (China) for China Scholarship Council financial support and The Sun Yat-Sen Innovative Talents Cultivation Program for Doctoral Graduate Student.

#### Appendix A. Supplementary material

Supplementary data related to this article can be found online at <http://dx.doi.org/10.1016/j.jpowsour.2013.03.083>.

#### References

- [1] L.Y. Yuan, X. Xiao, T.P. Ding, J.W. Zhong, X.H. Zhang, Y. Shen, B. Hu, Y.H. Huang, J. Zhou, Z.L. Wang, *Angew. Chem. Int. Ed.* 51 (2012) 4934–4938.
- [2] M.F. El-Kady, V. Strong, S. Dubin, R.B. Kaner, *Science* 335 (2012) 1326–1330.
- [3] L.F. Shen, X.G. Zhang, E. Uchaker, C.Z. Yuan, G.Z. Cao, *Adv. Energy Mater.* 2 (2012) 691–698.
- [4] Q.V. Overmeere, K. Kerman, S. Ramanathan, *Nano Lett.* 12 (2012) 3756–3760.
- [5] X.H. Lu, T. Zhai, X.H. Zhang, Y.Q. Shen, L.Y. Yuan, B. Hu, L. Gong, J. Chen, Y.H. Guo, J. Zhou, Y.X. Tong, Z.L. Wang, *Adv. Mater.* 24 (2012) 938–944.
- [6] L.Y. Yuan, X.H. Lu, X. Xiao, T. Zhai, J.J. Dai, F.C. Zhang, B. Hu, X. Wang, L. Gong, J. Chen, C.G. Hu, Y.X. Tong, J. Zhou, Z.L. Wang, *ACS Nano* 6 (2012) 656–661.
- [7] Y.J. Kang, H. Chung, C.H. Han, W. Kim, *Nanotechnology* 23 (2012) 065401–065407.
- [8] X.L. Wang, G. Li, Z. Chen, V. Augustyn, X.M. Ma, G. Wang, B. Dunn, Y.F. Lu, *Adv. Energy Mater.* 1 (2011) 1089–1093.
- [9] H.J. Liu, J. Wang, C.X. Wang, Y.Y. Xia, *Adv. Energy Mater.* 1 (2011) 1101–1108.
- [10] G. Wang, X. Sun, F. Lu, H. Sun, M. Yu, W. Jiang, C. Liu, J. Lian, *Small* 8 (2012) 452–459.
- [11] Y. Qiu, X. Zhang, S. Yang, *Phys. Chem. Chem. Phys.* 13 (2011) 12554–12558.
- [12] D.F. Sun, X.B. Yan, J.W. Lang, Q.J. Xue, *J. Power Sources* 222 (2013) 52–58.
- [13] S.L. Candelaria, B.B. Garcia, D.W. Liu, G.Z. Cao, *J. Mater. Chem.* 22 (2012) 9884–9889.
- [14] L. Chen, L.J. Sun, F. Luan, Y. Liang, Y. Li, X.X. Liu, *J. Power Sources* 195 (2010) 3742–3747.
- [15] X.H. Lu, X. Huang, S.L. Xie, T. Zhai, C.S. Wang, P. Zhang, M.H. Yu, W. Li, C.L. Liang, Y.X. Tong, *J. Mater. Chem.* 22 (2012) 13357–13364.
- [16] D.S. Yuan, J.X. Chen, J.H. Zeng, S.X. Tan, *Electrochem. Commun.* 10 (2008) 1067–1070.
- [17] R.B. Rakhi, W. Chen, D. Cha, H.N. Alshareef, *Nano Lett.* 12 (2012) 2559–2567.
- [18] X.H. Lu, D.Z. Zheng, T. Zhai, Z.Q. Liu, Y.Y. Huang, S.L. Xie, Y.X. Tong, *Energy Environ. Sci.* 4 (2011) 2915–2921.
- [19] Z.B. Lei, J.T. Zhang, X.S. Zhao, *J. Mater. Chem.* 22 (2012) 153–160.
- [20] C.L. Xu, Y.Q. Zhao, G.W. Yang, F.S. Li, H.L. Li, *Chem. Commun.* (2009) 7575–7577.

- [21] S.L. Chou, J.Z. Wang, S.Y. Chew, H.K. Liu, S.X. Dou, *Electrochem. Commun.* 10 (2008) 1724–1727.
- [22] Y.B. He, G.R. Li, Z.L. Wang, C.Y. Su, Y.X. Tong, *Energy Environ. Sci.* 4 (2011) 1288–1292.
- [23] M. Ghaemi, F. Ataherian, A. Zolfaghari, S.M. Jafari, *Electrochem. Acta* 53 (2008) 4607–4614.
- [24] X.H. Lu, G.M. Wang, T. Zhai, M.H. Yu, J.Y. Gan, Y.X. Tong, Y. Li, *Nano Lett.* 12 (2012) 1690–1696.
- [25] L.H. Bao, J.F. Zang, X.D. Li, *Nano Lett.* 11 (2011) 1215–1220.
- [26] S.M. Dong, X. Chen, L. Gu, X.H. Zhou, L.F. Li, Z.H. Liu, P.X. Han, H.X. Xu, J.H. Yao, H.B. Wang, X.Y. Zhang, C.Q. Shang, G.L. Cui, L.Q. Chen, *Energy Environ. Sci.* 4 (2011) 3502–3508.
- [27] J.A. Yan, E. Khoo, A. Sumboja, P.S. Lee, *ACS Nano* 4 (2010) 4247–4255.
- [28] C.C. Hu, K.H. Chang, Y.T. Wu, C.Y. Hung, C.C. Lin, Y.T. Tsai, *Electrochem. Commun.* 10 (2008) 1792–1796.
- [29] F. Buciuman, F. Patcas, R. Craciun, D.R.T. Zahn, *Phys. Chem. Chem. Phys.* 1 (1999) 185–190.
- [30] C.M. Julien, M. Massot, C. Poinsignon, *Spectrochim. Acta A Mol. Biomol. Spectrosc.* 60 (2004) 689–700.
- [31] M. Chigane, M. Ishikawa, *J. Electrochem. Soc.* 147 (2000) 2246–2251.
- [32] M. Oku, K. Hirokawa, S. Ikeda, *J. Electron Spectrosc. Relat. Phenom.* 7 (1975) 465–473.
- [33] J.K. Chang, M.T. Lee, W.T. Tsai, M.J. Deng, I.W. Sun, *Chem. Mater.* 21 (2009) 2688–2695.
- [34] W. Yan, T. Ayyvazian, J. Kim, Y. Liu, K.C. Donovan, W. Xing, Y. Yang, J.C. Hemminger, R.M. Penner, *ACS Nano* 5 (2011) 8275–8287.
- [35] Z. Li, J. Wang, X. Liu, S. Liu, J. Ou, S. Yang, *J. Mater. Chem.* 21 (2011) 3397–3403.
- [36] H. Jiang, T. Sun, C.Z. Li, J. Ma, *J. Mater. Chem.* 22 (2012) 2751–2756.
- [37] H. Zhu, X. Wang, X. Liu, X. Yang, *Adv Mater.* 24 (2012) 6524–6529.
- [38] H. Xia, J.K. Feng, H.L. Wang, M.O. Lai, L. Lu, *J. Power Sources* 195 (2010) 4410–4413.